Nuclear Materials and Energy 38 (2024) 101589

Contents lists available at ScienceDirect

Nuclear Materials and Energy

journal homepage: www.elsevier.com/locate/nme

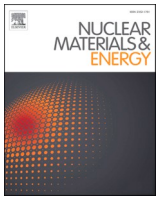

Deuterium retention and transport in ion-irradiated tungsten exposed to deuterium atoms: Role of grain boundaries

S. Markelj [a,*], J. Zavašnik [a], A. Šestan [a], T. Schwarz-Selinger [b], M. Kelemen [a], E. Punzón-Quijorna [a], G. Alberti [c], M. Passoni [c,d], D. Dellasega [c,d]

[a] Jožef Stefan Institute, Ljubljana, Slovenia
[b] Max-Planck-Institut für Plasmaphysik, Garching, Germany
[c] Dipartimento di Energia, Politecnico di Milano, Milano, Italy
[d] Istituto per la Scienza e Tecnologia dei Plasmi, CNR, Milano, Italy

ARTICLE INFO

Keywords:
D atoms
Grain boundaries
Transport
Displacement damage
Retention
Tungsten

ABSTRACT

The influence of grain boundaries on deuterium (D) retention and transport was investigated in nanocrystalline tungsten (W) by exposing the samples to sub eV D atoms. Thin tungsten films with nanometer-sized grains were produced by pulsed laser deposition on tungsten substrates. Their grain size was increased up to one micrometer by thermal annealing in vacuum up to 1223 K. Irradiation damage was created by 20 MeV W ions at 290 K. The transmission electron microscopy analysis showed one order of magnitude larger dislocation density in nanometer-grained samples compared with the larger-grained samples. The samples were after W irradiation exposed to 0.3 eV D atoms at 600 K. D retention and D depth profiles were measured by nuclear reaction analysis. In the as-deposited nanometer-grained samples, D populated the damaged region more than three times faster than in the samples with larger grains, indicating that grain-boundaries increase D transport through the material. The concentration of defects was assessed by the final D concentration in the samples. The sample with the smallest grain size showed slightly larger D concentration in the irradiated area, but the difference in the D concentration was not substantial between different-grained samples. A large D concentration in the non-irradiated nanometer-grained sample was measured which is an indication for a high defect density in the initial material. From our observations, it can be postulated that the nanocrystalline microstructure did not substantially influence the generation of irradiation-induced defects by defect annihilation at grain boundaries.

1. Introduction

Among the materials composing the first wall, facing the thermonuclear plasma, tungsten (W) is considered the material of choice in the areas exposed to high particle fluxes and thermal power loads. In addition to particle and thermal loads, W components have to face deuterium–tritium fusion generated neutron irradiation that will create displacement damage, influencing material properties, such as material ductility and strength. Fuel (deuterium and tritium) retention in future fusion devices is an important topic due to the safety and tritium self-sufficiency. It was shown that hydrogen isotope retention in displacement damaged tungsten is increased by several orders of magnitude, leading to fuel retention in at. % range [1,2]. There is a debate how grain size and grain boundaries (GBs) in tungsten , can influence the generation of radiation damage, fuel retention and transport. It was shown in the literature that large density of grain boundaries could, depending on the irradiation conditions and the material, decrease the survival probability of vacancies and self-interstitials in different materials [3,4,5]. In materials such as Cu, the nanocrystalline microstructure with a high grain boundary density improves radiation tolerance [3,5]. For tungsten, the available literature data presents conflicting findings. Some experiments suggest an improved radiation tolerance [6,7], while others claim the opposite, showing an increased number of vacancies in nanostructured materials as compared to single crystal tungsten [8,9].

With respect to hydrogen isotope (HI) interaction with GBs, it was shown that GBs could also influence the HI transport and retention. Again, there is much debate about the possible conflict between the fact that GBs can be either a trap and/or a short-circuit for diffusion. For tungsten, theory and experiment showed that GBs can provide high diffusion pathways for hydrogen, where the diffusion barrier is lower

* Corresponding author.
E-mail address: sabina.markelj@ijs.si (S. Markelj).

https://doi.org/10.1016/j.nme.2024.101589
Received 15 November 2023; Received in revised form 5 January 2024; Accepted 8 January 2024
Available online 9 January 2024

than in the bulk of tungsten [10,11,12,13]. On the other hand, some studies show that the diffusion of hydrogen in nanocrystalline W is trap dominated, meaning that GBs act as traps for hydrogen [14]. The calculated maximum values for H trapping on a GB interface [15,16,14] are very close to the trapping energy of H on a vacancy [16]. In contrast, some theoretical predictions for H trapping show that although H can potentially be trapped at the GBs, it is more likely to be trapped in vacancies than in the GBs [10]. A similar conflict exists for other metals, showing that some grain boundaries are potential hydrogen traps and that hydrogen diffusion is accelerated in some GBs [17,18,19,20]. The experimental results of deuterium (D) retention in different nanostructured tungsten coatings show that the D concentration at the radiation-induced defects is not microstructure dependent and is the same regardless of the W crystal structure [21].

The effect of microstructure on the generation of radiation damage was studied previously by our group in samples with the smallest grain size of 1–2 μm [22]. To create displacement damage, we have used high-energy W ions, which are a good proxy for neutron irradiation [23,24], excluding transmutation, helium production and, most importantly, activation of the material. The quantification of defect formation was assessed through decoration by deuterium (D), as lattice defects serve as capture sites for HIs with considerably higher de-trapping energy than the energy required for HI diffusion between solute interstitial sites. Therefore, the HI concentration can be treated as a measure of the defect content present in the material. No significant difference was observed between a single crystal, a recrystallized polycrystal with 10–50 μm grain size and a hot rolled polycrystal with a micrometer grain size, and all samples showed similar final D concentrations in the damage zone [22].

We expand this investigation by reducing the W grain size to the nanometer range to study the microstructure of the films and how the grain size and GB density affect the D retention and transport. The concentration of defects was assessed by exposing samples to sub-eV energy D atoms at 600 K. This populates the defects created by the W irradiation and the defects possibly existing due to the manufacturing process. Moreover, the study presented here is also an extension of the study in which similar nanocrystalline films were subjected to 300 eV D ions at 450 K [25]. By comparing the results of both studies, we gain insight into the influence of GBs on D retention, and consequently on defect density, by populating defects at different exposure temperatures. In addition, by comparing the present results from 0.3 eV D atoms with results from 300 eV ions [25] we can derive to which extent the observed effects are due the surface or due to the bulk.

2. Sample production and experiment

W films were deposited on polycrystalline W (poly-W) substrates with dimensions 15x15 mm^2 by pulsed laser deposition (PLD) at the Energy Department of Politecnico di Milano [26]. Prior to deposition, poly-W substrates with grain size of about few micrometers were polished and cleaned with isopropyl alcohol. The native W oxide at the surface has intentionally not been removed to prevent any influence of the W substrate on the growth and crystallinity of the W films. In the PLD process, a laser pulse with a fluence of 15 J/cm^2 hits a W target, and due to the laser-matter interaction, W is ablated at high energy (100 eV/atom) and expands in the vacuum chamber (base pressure 10^{-3} Pa). The W species impinge on a poly-W substrate placed 7 cm away from the target at room temperature. No intentional heating was applied. The W film grows with a 15 nm/min deposition rate, and W films with 3 μm thickness ± 10 % (mean on the whole surface) were deposited. The as-deposited sample with nanometer-size grains was processed without further modifications. The other two samples were vacuum-annealed (base pressure 5×10^{-5} Pa) by an internal heater at 1023 and 1223 K for 2 h of dwell time and at 20 °C/min heating and cooling ramps, to tailor the grain size in the 100's nm range and micron-size range. The grain size increase with annealing temperature was studied in detail in [27].

All three variants of samples were irradiated by 20.3 MeV W ions to a fluence of 7.8×10^{17} Wm^{-2} at room temperature (300 K) in the TOF beamline at Max-Planck-Institut für Plasmaphysik (IPP), Garching [28]. To establish undamaged references, half of each sample was covered during W irradiation. For the chosen energy of 20.3 MeV, SRIM 2008.04 [29] predicts for bulk tungsten a displacement damage down to a depth of 2.3 μm with a peak at 1.35 μm, as depicted in Fig. 7. Evaluating the 'vacancy.txt' output of the 'Quick Calculation of Damage Option' of SRIM 2008.04 with a displacement threshold energy E_D of 90 eV, this converts to a primary damage dose in the damage peak of 0.23 dpa. The damage dose was chosen to achieve defect saturation for hydrogen-free W. Namely, studies with comparable W material and damaging procedure showed that D retention saturates at a damage level of ≈ 0.1 dpa [23,2], confirmed recently by parameter-free modelling [30]. Consequently, a flat distribution of defects and constant D retention through the damaged zone down to about 2 μm is expected.

Following W irradiation, the W samples underwent exposure to D in the in-situ Ion Beam Analysis (INSIBA) chamber at the 2 MV tandem accelerator at Jožef Stefan Institute (JSI) [31]. For this purpose, the damaged W samples were exposed to a neutral atomic deuterium beam with an approximate energy of 0.3 eV [31,32]. The atomic deuterium beam was generated through thermal dissociation of hydrogen molecules within a hot capillary, utilizing a commercial hydrogen atom beam source (HABS, MBE). The exposure was conducted at a sample temperature of 600 K allowing the D atoms to populate solely the high-energy traps (de-trapping energies exceeding 1.60 eV), as previously demonstrated [33]. The average D atom flux was $j = 1.5 \times 10^{18}$ D/m^2s. The D atom beam was impacting the sample at an angle of 51° with respect to the sample surface normal. Due to the relatively high exposure temperature of 600 K small annealing of the defects takes place. In a preceding study a reduction of approximately 10 % of the D total amount or D concentration was observed at this temperature [34,33]. This temperature was selected to obtain comparable data with previous experiments [22]. Lower exposure temperatures such as the one used for the 300 eV/D ion exposures (450 K) [25] are not possible with low energy D atoms because they hardly overcome the surface barrier to penetrate into the bulk even for very long exposure times of 120 h [35].

The D depth profiles were obtained using ^{3}He nuclear reaction analysis (NRA) at specific time intervals during the D atom exposure and at the end of the exposure. During the exposure, the D atom beam size is such that it covers the whole W sample. The samples were exposed until the damaged area was fully saturated, with the D concentration homogeneous over the damaged layer. The average D atom flux on the sample was $(1.5 \pm 0.2) \times 10^{18}$ D/m^2s as determined by erosion of a thin amorphous hydrogenated-carbon film on a Si wafer [see [31] and references therein]. The maximum exposure time for 0.3 eV D atoms was 96 h, corresponding to a D fluence of 5.2×10^{23} D/m^2. The final measurement was taken after the stop of D-atom exposure. Due to the potential thermal D-release during sample cooling at the end of exposure [36], all samples were first cooled and when the temperature had dropped approximately 100 degrees below the exposure temperature, the D-atom exposure was stopped. The $D(^3He, p)^4He$ nuclear reaction was used [37] to analyze the retained deuterium with six different ^{3}He energies ranging from 700 keV to 4.3 MeV, with a 2 mm ^{3}He beam size. The NRA detector was positioned at an angle of 160° with respect to the probing beam. Probing beam was impacting the sample parallel to the surface normal. Absolute quantitative local information on the D concentration down to 7.2 μm was obtained by deconvoluting all measured proton energy spectra simultaneously using the software NRADC [38] and SIMNRA 6.02 [39]. We also determined the oxygen concentration in the layers using the $^{16}O(^3He,p_0)^{18}F$ reaction at ^{3}He energies above 2.5 MeV. The cross-section by Guitart Corominas and Schwarz-Selinger [40] was used for absolute quantification of the oxygen. The maximum information depth for oxygen is about 3 μm for a ^{3}He energy of 4.2 MeV.

The X-ray diffraction (XRD) spectra of the native and implanted

tungsten samples were obtained using an Empyrean X-ray diffractometer in θ-2θ geometry. The X-ray source uses the Cu Kα line (λ = 1.5406 Å) generated by an impinging electron beam that was set to 40 mA at 45 kV. The scan range was set from 2θ = 35° to 135°, with a step size of 0.013° and a scan step time of 398 s. The penetration depth of the X ray is approximately 3 μm. The Williamson-Hall analysis was used to determine the average crystallite size and average micro-strain in the thin film samples, evaluating the width of the diffraction peaks. This technique correlates the broadening of the X-ray diffraction peaks with the crystallite size and micro-strain in the material. The equation used to construct the Williamson-Hall plot [41] is as follows: $\beta_{hkl} \cos\theta = k\,\lambda\,/D + 4\varepsilon \sin\theta$, were β_{hkl} is the full width at half maximum (FWHM) of the X-ray diffraction peak corresponding to a specific crystallographic plane (*hkl*), θ is the Bragg angle, representing the angle of incidence of the X-ray beam on the sample, λ stands for the wavelength of the X-ray, D signifies the crystallite size of the material, k is the Scherrer constant (0.94), and ε is the micro-strain present in the sample. The instrumental peak broadening was determined using a Si standard. For the XRD diffractograms analysis we applied HighScore Plus software and CrystalMaker software. XRD, using the Williamson-Hall analysis method, is the standard technique used to study the crystallite size and micro-strain changes in the material due to ion irradiation e.g. [42,43].

The grain size analysis of thin films was estimated by a dual-beam focused ion beam / scanning electron microscope (FIB-SEM, Helios Nanolab 650i, FEI) operating at 15 kV. For atomic-scale observations, crystal structure analysis, and phase-composition assessment, we employed a 200 keV transmission electron microscope (TEM, JEM-2100, JEOL Inc.) equipped with a slow-scan CCD camera (Orius SC1000, Gatan Inc.) and a scanning TEM (ARM 200CF, JEOL Inc.). Thin lamellae for the scanning/transmission electron microscopy (S/TEM) analyses were prepared by FIB lift-out technique.

The D desorption spectra from the samples were measured 21 months after the D atom exposures and NRA analysis using thermal desorption spectroscopy (TDS), keeping the samples in a desiccator in the meantime. The TDS measurement was performed in a quartz tube of the TESS set-up at IPP [44,45] using a tubular furnace. A 3 K/min linear heating ramp up to 1010 K and a > 30 min hold at the highest temperature was applied. The desorbed gases were measured with a Pfeiffer/Inficon DMM 422 quadrupole mass spectrometer (QMS). The following 15 mass channels were recorded: $m/z = 1$, 2, 3, 4, 12, 14, 16, 17, 18, 19, 20, 28, 32, 40, and 44. For the quantitative analysis, the QMS signal for D_2 was calibrated after each temperature ramp with a leak bottle from Laco Technologies with a flow of 1.22×10^{14} D_2/s and a stated accuracy of 4.6 %. The calibration factor for HD was determined by flowing HD through an orifice of known size from a calibrated volume of known absolute pressure (measured with a capacitance manometer and spinning rotor gauge) into the mass spectroscopy vessel. Based on the pressure recording of a calibrated spinning rotor gauge the calibration factor for HD molecules per measured QMS count was 62 % of the one derived for D_2. To determine the amount of D desorbed during the measurement, masses 3 amu/q and 4 amu/q, corresponding to HD and D_2 molecules, respectively, were summed up. There was also some signal increase at masses 19 amu/q and 20 amu/q, corresponding to HDO and D_2O. Detailed description of the water calibration technique is given in [46]. The D signal coming from the water was added to the total D desorbed signal. During the TDS measurements, the sample temperature was monitored directly using a shielded thermocouple in direct contact with the sample. Since samples were only half-irradiated by W ions, they needed to be cut prior to the TDS to be able to perform measurements on both halves separately. Cutting was done with a circular saw under water to avoid heating. Cleaning was performed in ultrasonic bathes of acetone and ethanol.

3. Microstructural investigation

3.1. Scanning electron microscopy (SEM) analysis

The thickness and grain size of the deposited W samples were analysed by SEM and FIB-made cross-sections after the D atom exposures at 600 K. It is important to note that grain coarsening occurs at approximately 800 K [27]; hence, these measurements represent the initial grain size distributions of the material. SEM micrographs of the sample's surfaces (top view) are shown in Fig. 1 for all the different-grained samples. Low magnification images (top) show generally the flat W surface. In the high magnification images (below) the individual grains are visible in the case of "as-deposited", referred to as the *nanometer-grained (nG) sample* (Fig. 1a) and *hundred-nanometer-grained (HnG) sample*, annealed at 1023 K for 2 h (Fig. 1b). Different roughness features, that are related to the grain growth are visible in the case of *micrometer-grained (mG) sample*, annealed at 1223 K for 2 h, Fig. 1c. The SEM cross-section micrographs are shown in Fig. 2, for all studied samples. In all cases the estimated film thickness is approximately 2.5–3 μm. The grain size for individual films was measured based on the diffraction contrast in FIB-SEM cross-section micrographs. For the *nG sample* the estimated mean grain size is 25 nm, Fig. 2a. The *HnG sample*, was annealed at 1023 K for 2 h, which resulted in grain growth up to 300 nm in size with a mean distribution at 80 nm (Fig. 2b). The third sample, the *mG sample*, was annealed at 1223 K for 2 h, resulting in μm-sized grains with a mean grain size of 0.5 μm (Fig. 2c).

3.2. X-ray diffraction (XRD) analysis

The deposited thin films of undamaged and W-damaged regions of each sample after D exposure were analyzed by XRD. The XRD diffractograms of undamaged (nG, HnG, mG) and W-damaged (nG-d, HnG-d, mG-d) W thin film samples are presented in Fig. 3a. They confirm that the deposited thin films layer is an α-bcc W with (1 1 0) preferential orientation, as established in previous XRD studies [26].

The magnified XRD diffraction peaks of the W (1 1 0) crystal plane are shown for undamaged and W-damaged halves of the samples in Fig. 3b. For the nG sample, we can observe a broad and diffused diffraction peak. This peak grows and narrows by increasing the thin films grain size. Broadening of the diffraction peak, compared to the undamaged counterparts, was observed after W-damaging in all three sets of samples.

The results of the Williamson-Hall analysis are summarized in Fig. 3c. For the undamaged *nG sample*, the calculated crystallite size is 36 nm. Crystallite size slightly increased in the W-damaged half, up to 48 nm. The micro-strain in the native nG sample reaches 2×10^{-3} and remains the same in the W-damaged half. For the HnG sample, annealing at 1023 K for 2 h increased the crystallite size to 72 nm and decreased the micro-strain to 0.7×10^{-3}. The W-damaged half of the HnG sample shows an increase in crystallite size to 144 nm and micro-strain up to 0.9×10^{-3}. The mG sample was annealed at 1223 K for 2 h, causing the crystallite size to increase further to 289 nm and to decrease the micro-strain to 0.2×10^{-3}. On the W-damaged half of the mG sample, a decrease of crystalline size to 144 nm is observed and an increase in micro-strain to a value of 0.5×10^{-3}. From the results of XRD analysis, we can conclude that annealing of "as deposited" nG W thin films leads to crystallite growth and a reduction of micro-strain. Additionally, XRD analysis indicates that the effect of W-damaging is more pronounced in the materials with larger crystallite sizes where the micro-strain increases due to self-damaging. The crystallite size calculated from XRD analysis is in reasonable agreement with the SEM estimations based on the diffraction contrast. In the XRD diffractogram of the mG sample we can observe in the (1 1 0) crystal plane diffraction (Fig. 3b) that K-alpha 1 (Kα1) and K-alpha 2 (Kα2) are further apart at low 2θ angles. In all samples, two small intensity peaks were observed at about 36° and 77° 2θ (marked with a star in Fig. 3a), which we assume to be one of the

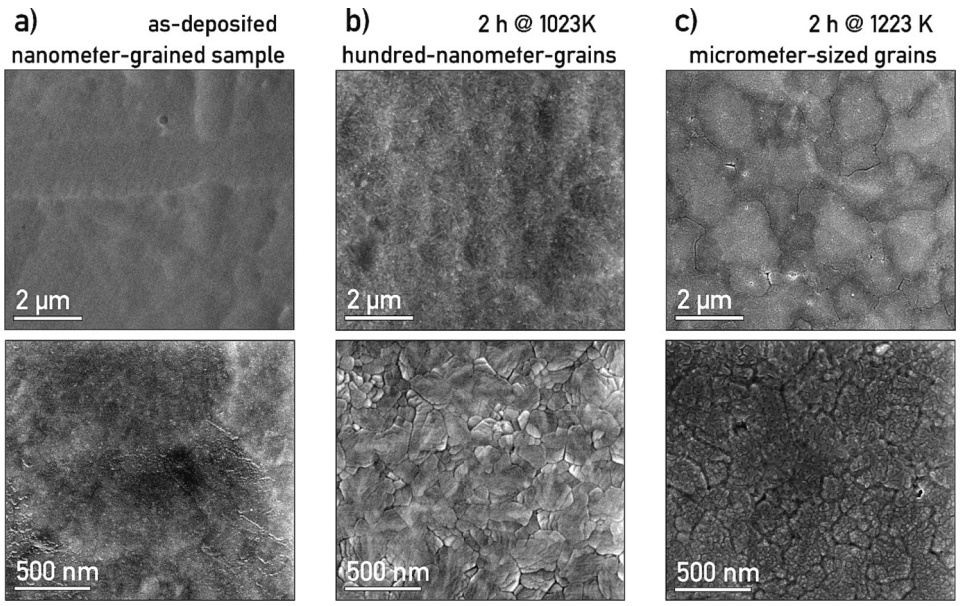

Fig. 1. SEM micrographs of the surface for samples with different grain sizes: a) as-deposited film – nanometer grained (nG) sample; b) sample annealed at 1023 K for 2 h – hundred-nanometer grained (HnG) sample; and c) sample annealed at 1223 K for 2 h - the micrometer grained (mG) sample.

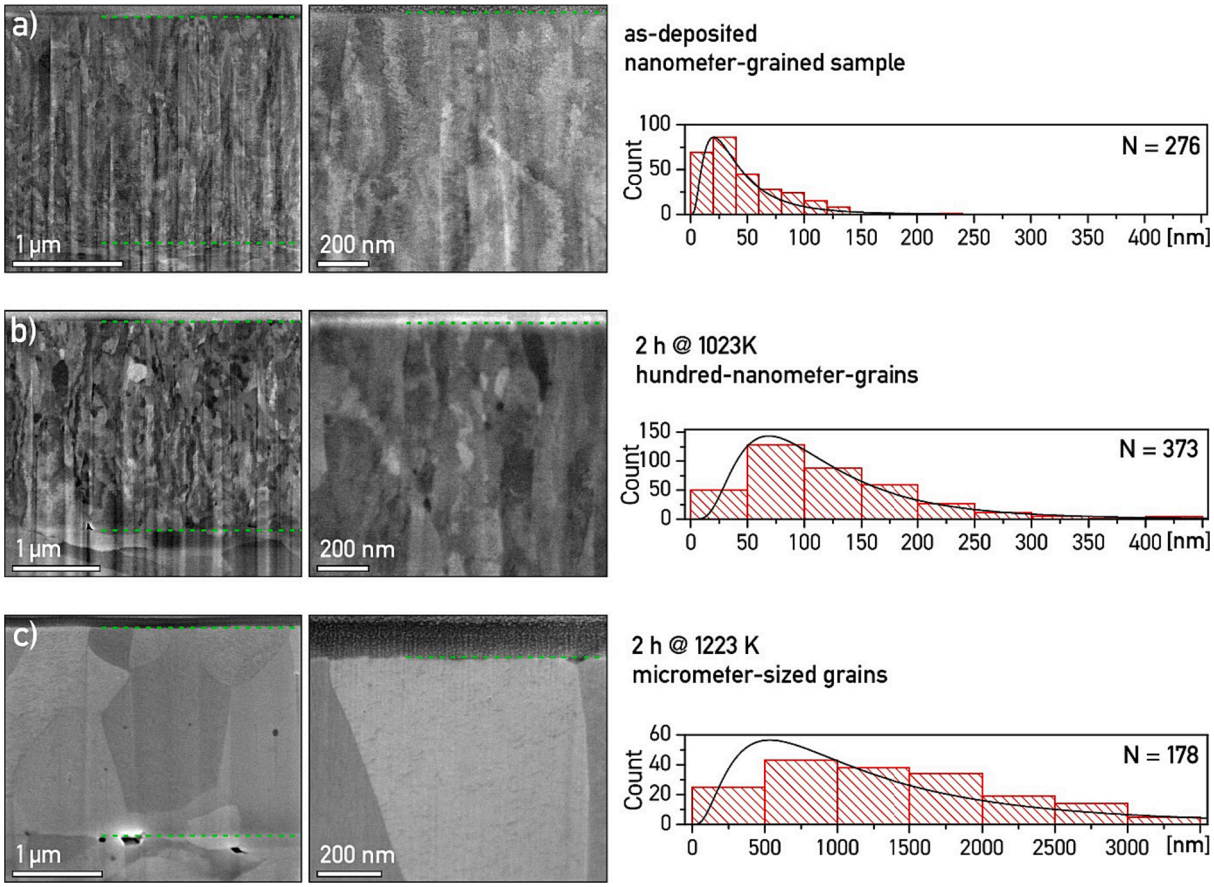

Fig. 2. SEM micrographs of cross-sections for samples with different grain sizes: a) as-deposited film – nG sample; b) sample annealed at 1023 K for 2 h –HnG sample; c) sample annealed at 1223 K for 2 h – mG sample with the corresponding grain size distribution histogram. (a-c) cross-section SEM micrographs with marked deposited W layer (green dash lines) on W substrate, topped by protective Pt deposit for FIB cutting, with corresponding magnified near-surface details. (For interpretation of the references to colour in this figure legend, the reader is referred to the web version of this article.)

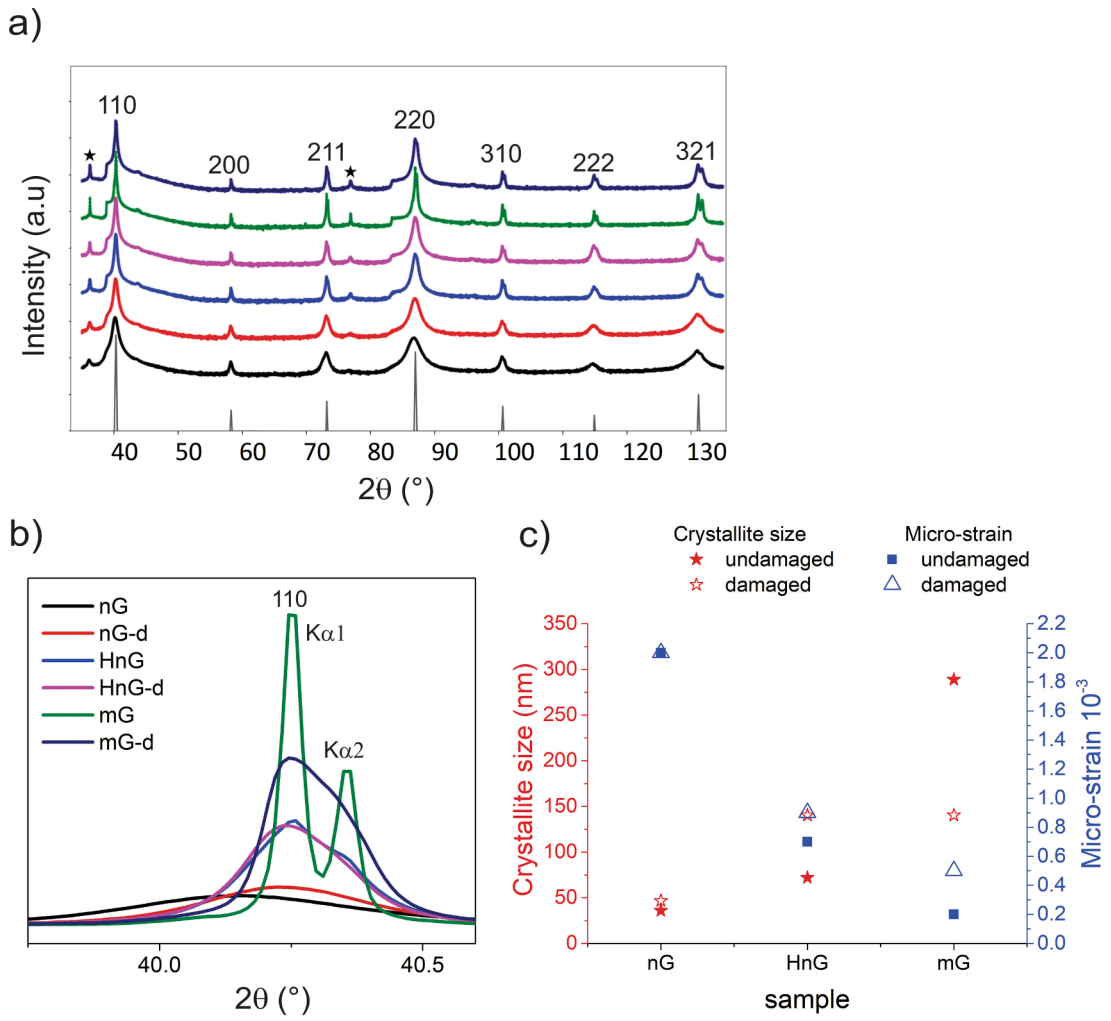

Fig. 3. A) comparison of simulated bcc W XRD diffractogram (grey peaks) and experimental XRD diffractograms of undamaged (nG, HnG, mG) and W-damaged (nG-d, HnG-d, mG-d) W thin film samples. b) Magnified XRD region around W (1 1 0) crystal plane diffraction peak. c) The plot of calculated average micro-strain and crystallite size for undamaged and W-damaged thin films samples. The average crystallite size in the undamaged samples is marked by a full red star, and in the W-damaged samples is marked by an empty red star. The calculated average micro-strain in the undamaged samples is marked by a full blue square, and in the W-damaged samples is marked by an empty blue triangle. (For interpretation of the references to colour in this figure legend, the reader is referred to the web version of this article.)

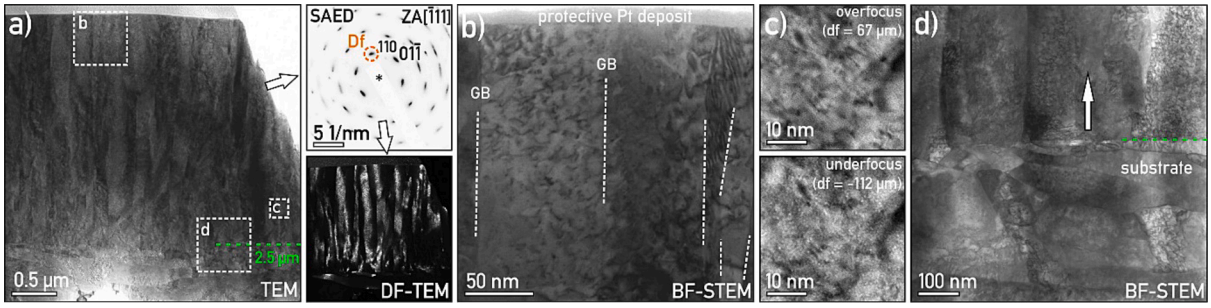

Fig. 4. a) TEM micrograph on the damaged half of the **nanometer-grained (nG) sample** (as-deposited film), with corresponding SAED indexed for W and with marked aperture position for the corresponding dark-field (Df-TEM) TEM micrograph. Small squares labelled b-d are showing the areas where figures b-d are taken. **b)** Bright-field STEM (BF-STEM) micrograph of a near-surface region with marked grain boundaries (GB), with visible numerous dislocations (DLs). **c)** over- and under-focus micrograph pair of nano-scale voids. **d)** BF-STEM micrograph of an interface between deposited W film and W substrate, with visible pillar-like microstructure and DLs network; arrow marks the ⟨1 1 0⟩ direction.

tungsten oxide rich phases [47].

3.3. Transmission electron microscopy (TEM) analysis

TEM analysis of the specimen was done on FIB-made thin samples, yielding an electron-transparent region of ≈ 7 × 10 μm^2 in size. A

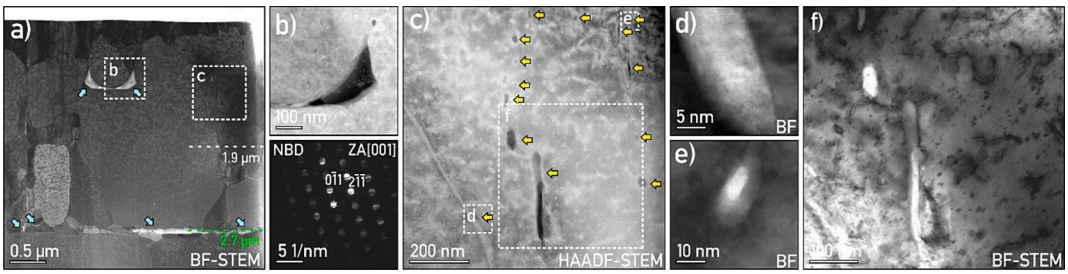

Fig. 5. a) BF-STEM micrograph on the damaged half of the **hundred-nanometer grained (HnG) sample**, annealed for 2 h at 1023 K; blue arrows mark oxide phases. The indicated squares show the locations of figures b and c. **b)** High-angle annular dark field (HAADF)-STEM micrograph of crystalline WO_2 with corresponding nanobeam diffraction (NBD). **c)** HAADF-STEM micrograph of strings of voids, marked by yellow arrows. BF-STEM micrograph of crystalline WO_2 on **d)** grain boundary and **e)** crystalline WO2 found in bulk. **f)** BF-STEM micrograph of elongated voids with visible DLs network. The indicated squares shown in figure c show the locations of figures d-f. (For interpretation of the references to colour in this figure legend, the reader is referred to the web version of this article.)

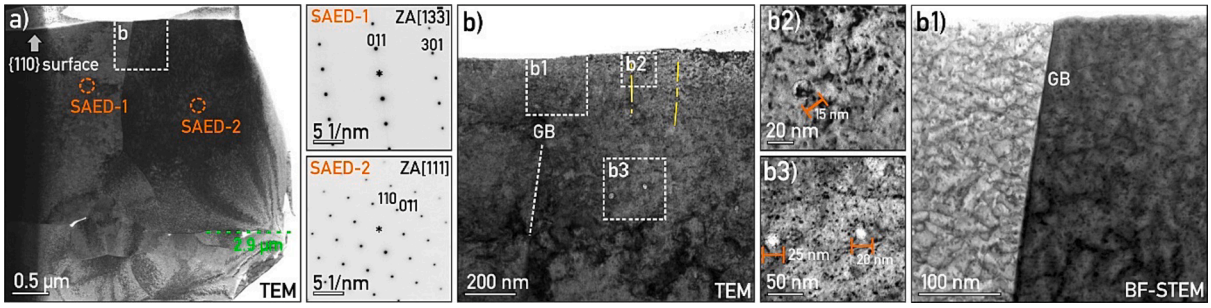

Fig. 6. (a) TEM micrograph of W-damaged half of the **micrometer-grained (mG) sample,** which was annealed for 2 h at 1223 K, with corresponding SAED indexed for pure W. **b)** TEM micrograph of the near-GB region, strings of nano-sized voids are indicated by white dashed lines. Two regions from **b2)** near-surface region and **b3)** from bulk are magnified. **b1)** BF-STEM micrograph of DLs network. Areas where figures b1-b3 are taken are shown in figure b.

comparison of the defects observed by STEM in the irradiated halves of the samples is shown in Figs. 4-6**.** The nG sample comprises pillar-like grains extending through the whole thickness of the deposited film of about 2.5 μm (Fig. 4a). Each pillar is ≈ 50 ± 14 nm wide and is composed of numerous slightly misaligned ≈20 nm big crystallites, reflecting in elongated diffraction spots in selected-area electron diffraction (SAED) and un-even, interrupted contrast in DF-TEM micrograph. Small grain size dictates the length of dislocation lines, and we observed a high density of short, irregular dislocations (DL). The estimated line-intercept DL density in the irradiated part is 1.67×10^{15} m^{-2} (Fig. 4b). We have also observed features similar to voids and bubble-like formations, about 0.5–1.5 nm in size, found throughout the length of the pillars and not only in the W irradiation area (Fig. 4c). Their overall presence indicates that they were rather created during the deposition procedure and not as a result of W ion irradiation. The grain shape and size abruptly change on the film-substrate interface, and we did not observe any orientation relationship between the substrate and the deposited film (Fig. 4d).

In the case of the HnG sample, the grains are significantly larger and are randomly orientated. We select an exceptionally large grain to analyse DL changes within the single grain, and we observe dense DL line structures in the first 1.9 μm. After that depth, the defect density reduces significantly (Fig. 5a). This depth is in good agreement with the SRIM-predicted damage depth. We observe longer and more scarce DL lines and scarce DL loops, which are mostly absent in the undamaged part of the deposited film. The estimated DL density is 2.59×10^{14} m^{-2}. One can also observe several quite large voids **(**Fig. 5b**)**; the larger ones are filled with crystalline WO_2 as determined by nano-beam diffraction (NBD) and Energy Dispersive X-Ray (EDS) analysis (in Supporting Information File) (Fig. 5d-e). Several smaller voids are elongated in the direction of the previous pillar-like interfaces (Fig. 5c, f). The crystalline WO_2 phase can also be found at the interface between the W substrate and deposited W film.

In the case of mG sample, the grains in the film are μm sized and are the same size as in the W substrate. The interface can only be estimated from the grain boundaries and oxide inclusions (Fig. 6a). The size of DL lines is similar as observed in the HnG sample (Fig. 6b1). Moreover, we observe irregular non-faceted voids, scattered in the bulk of the film at different depths. Their size is ≈25 nm (Fig. 6b, b2 and b3). The estimated DL density is 2.80×10^{14} m^{-2}.

From the fact that we observe larger voids for samples with larger grain size ((≈25 nm) in mG sample) we can suspect that the small voids (0.5–1.5 nm) observed in the nG sample coalesce during the annealing procedure done for tailoring the grain size. Similarly, the coalescence of voids in the undamaged half of the samples can be also observed by XRD, showing a decrease in the micro-strain when going from nanometer grain size to micrometer grain size sample.

As determined by ^{3}He NRA, the oxygen concentration in the W films is approximately 0.5–1 at.% down to 2 μm. After this depth we observe an increase in the O concentration to 3 at.% down to the analysis depth of about 3 μm. This is in good agreement with the TEM analysis which identifies the WO_2 phase at the interface. The measured oxygen concentration is the same in the as-deposited and annealed samples.

4. Deuterium retention results

The D depth profiles measured during the D atom exposure are shown in Fig. 7a for the nG sample. We can observe that already after 4 h, D reached the end of the damage zone at 2.3 μm, illustrated by the SRIM-calculated damage depth profile shown in Fig. 7. After 24 h, the maximum depth did not increase, but the D concentration increased in the damaged region to a value of 0.36 ± 0.002 at. %. After 48 h of exposure the D depth profile was very similar to the one after 24 h, suggesting that the damaged layer was saturated by D already after 24 h. At the end of the exposure, we also measured the D depth profiles on the undamaged half, shown in Fig. 7 with a grey line. The maximum D

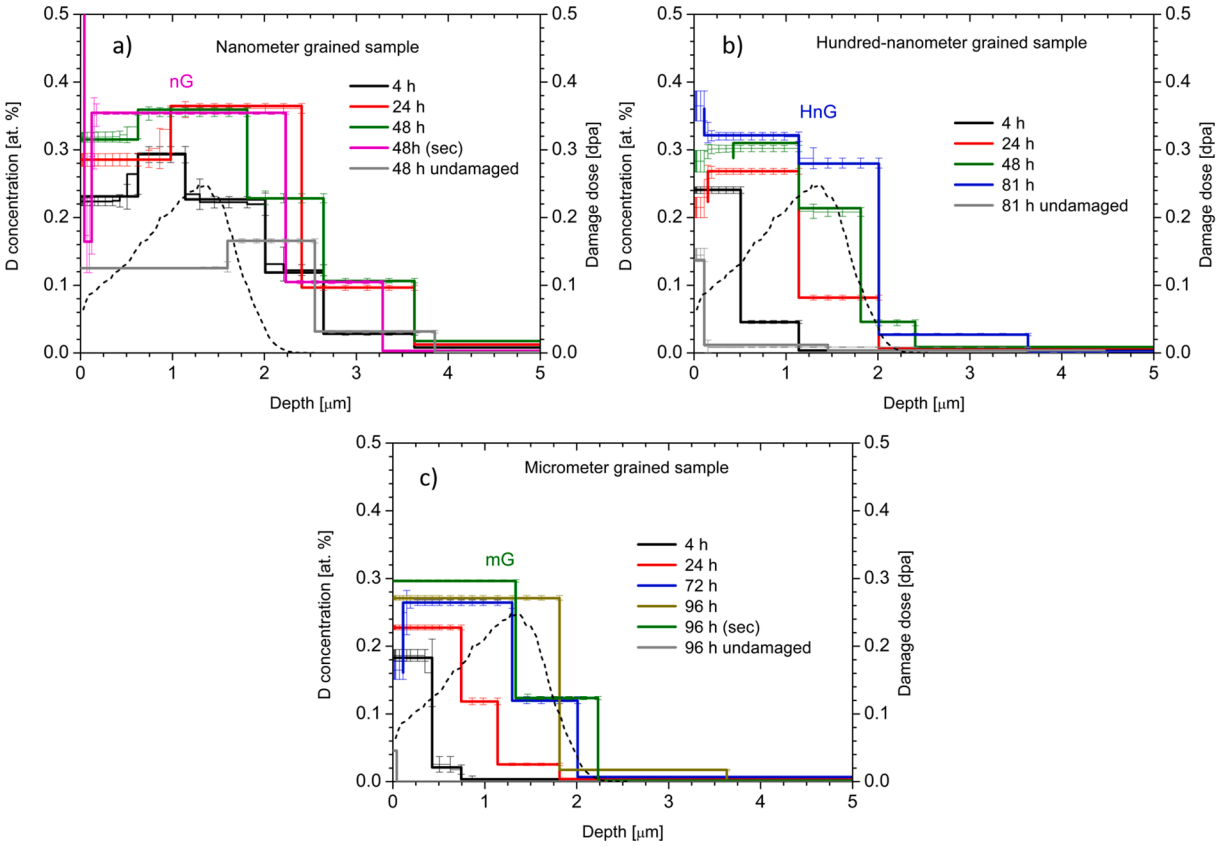

Fig. 7. D depth profiles measured at different exposure steps and at the end of the exposure to D atoms at 600 K on W-damaged halves: a) nG sample, b) HnG sample and c) mG sample. The D depth profiles obtained on the undamaged half of the sample at the end of D exposure are also shown as grey lines. SRIM calculated damage depth profile is also shown (dashed black lines) with a separate Y scale on the right. The depth profiles denoted by "sec" show measurements on a different spot on the sample.

concentration in the undamaged half was 0.13 ± 0.01 at. % and hence only about a factor of three smaller than the W-irradiated part of the sample. This is significantly larger as compared with polycrystalline bulk W samples. In hot-rolled polycrystalline W from Plansee, which was exposed to the same conditions, the maximum D concentration was 0.002 at. % [48] and hence a factor of 65 smaller.

In Fig. 7b, the D depth profiles obtained on the HnG sample are shown together with the SRIM-calculated damage depth profile. The sample was exposed to D atoms for 81 h. The diffusion front of D atoms went slowly inside and only after 81 h it penetrated to the end of the damaged range. The maximum D concentration on the damaged half was 0.32 ± 0.01 at. % and hence very similar to the damaged region of the nG sample. In addition, the undamaged part of the sample was also measured. The concentration in the undamaged half was 0.012 ± 0.006 at. % and hence more than one order of magnitude less than in the undamaged half of the nG sample.

We have performed the same time-dependent D depth profile measurements on the mG sample, Fig. 7c. We observe a similar trend of D penetration inside the bulk as compared with the HnG sample, where the diffusion front slowly moved in. The maximum D concentration in the damaged zone on the W-damaged half was 0.30 ± 0.005 at. % and hence again very similar to the other two types of samples. On the undamaged half, the D concentration was 0.005 ± 0.001 at. % in depth and, therefore, another factor of two less as compared with the HnG sample. However, even after 96 h of exposure, it looks like the D did not populate all the defects at 2 μm depth, suggesting that even longer exposure times would be needed to populate all the defects and finally reach a homogeneous D concentration down to about 2 μm. In the case of nG size and mG samples, we measured the D depth profile on a second spot, noted as "sec" in the graphs, to check for any effect of the probing ^{3}He beam [49].

The obtained D depth profiles are very similar to the one measured on the initial spot, so we can conclude that we do not observe any effect of the ^{3}He beam on the D retention.

Comparison of the D depth profiles between the W-damaged (full lines) and undamaged (dashed lines) half of the samples at the end of D atom exposure are shown in Fig. 8 for the three different-grained

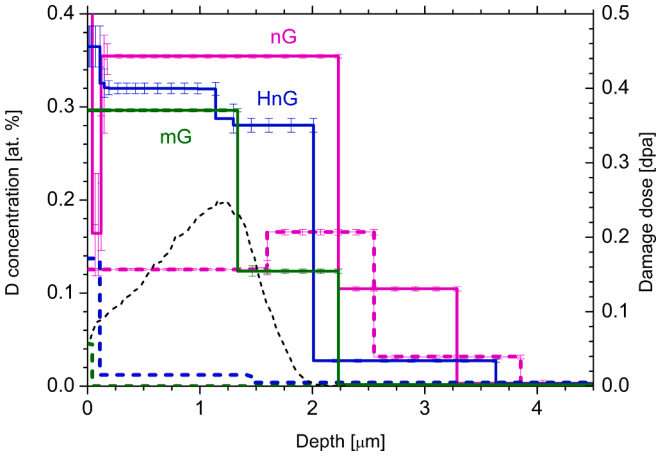

Fig. 8. D depth profiles measured at the end of the exposure to D atoms at 600 K (48 h for mG, 81 h HnG, 96 h mG) for all three types of samples from Fig. 7a, b and c for comparison. The D depth profiles obtained on the W-damaged halves are shown as full lines, and the undamaged halves are shown as dashed lines in the same colors. A SRIM-calculated damage depth profile is shown as dashed black line with a separate Y scale on the right.

samples. The small increase at the surface is due to the D adsorbed at the surface [31] and perhaps also to the cooling procedure we performed at the end of exposure [36], as described in section 2. The nG sample shows the highest D concentration for both the damaged (0.36 at. %) and undamaged half (0.13 at.%). The lowest D concentration for the W-damaged half occurs on the mG sample being 0.3 at. %. The concentration for the HnG sample is in between with 0.32 at. %. Obviously, the maximum D concentration is slightly larger for smaller grain size. However, if one subtracts the D concentrations obtained in the undamaged halves of the samples from the concentration for the damaged halves of the samples one obtains D concentrations of about 0.23 ± 0.02 at. % for the nG sample, 0.31 ± 0.02 at. % for the HnG sample and 0.29 ± 0.01 at. % for the mG sample. If we assume that the defects created by W ions are added to the initial defects present in the material due to the deposition process, we can conclude that 21 % fewer new defects were created in the case of the nG sample as compared to the mG sample. For the HnG sample, the difference is within the error bars. We can also conclude that the sample annealing at 1200 K efficiently reduces the initial deposition-induced defects, at least those responsible for D retention. Namely, the D concentration in the undamaged half of the samples is reduced by more than one order of magnitude when comparing the nG sample to the mG sample. From the decrease in D concentration we can assume the same decrease in defect concentration.

Fig. 9 shows the D areal densities (total amount of D within the ^{3}He-NRA information depth) as a function of exposure time for the W-damaged halves of the different-grained samples. It can be observed that the total amount of D for the nG sample was already at its maximum after 24 h, whereas for the other two cases it reaches its maximum only after about 80–96 h. It is possible that for these two samples the D saturation was not yet reached and additional exposure would be needed to completely populate the defects in the damaged layer. Therefore, the uptake in the nG sample was at least three times faster than in the HnG and mG samples. The amount of D in the undamaged halves is shown for comparison with the amount of D measured on the damaged halves subtracted from the amount of D on the undamaged halves.

The D desorption signal for the three different-grained samples is summarized in Fig. 10 as a function of the sample temperature during the TDS heating ramp. The spectra from the damaged and the

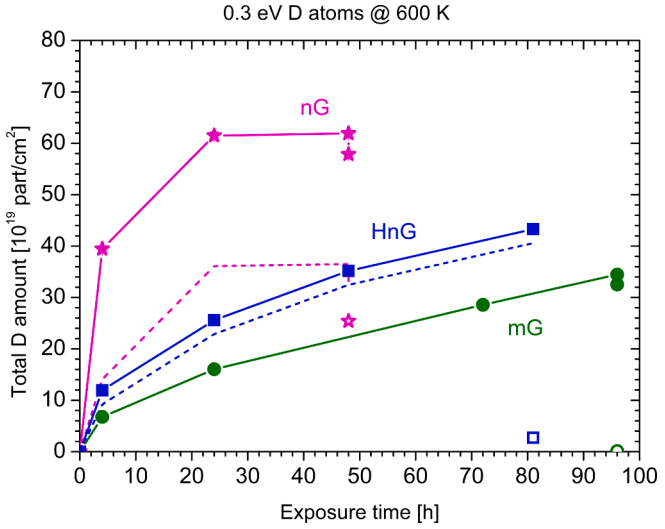

Fig. 9. Total D amounts within the ^{3}He-NRA information depth as a function of exposure time to D atoms with 0.3 eV for the W-damaged halves of the different-grained samples. The D retention in undamaged halves for all samples is shown as open symbols. Dashed lines show the D amount on damaged halves subtracted by the D amount measured on the undamaged halves for nG and HnG samples.

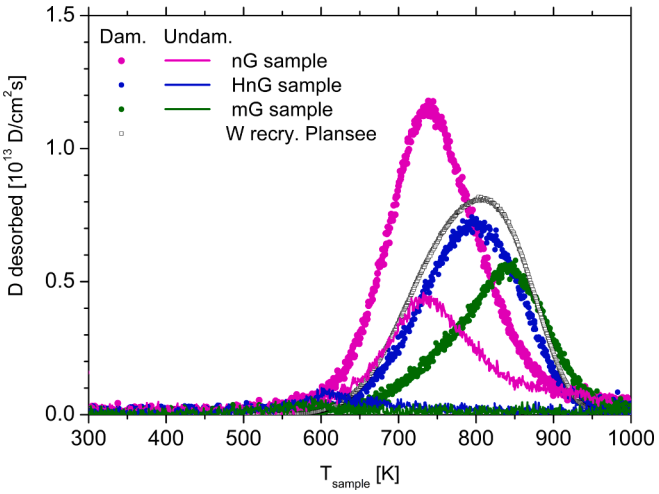

Fig. 10. D desorption spectra as a function of sample temperature for damaged and undamaged halves of samples. The furnace heating ramp was 3 K/min. We also compare a D desorption spectrum obtained from a recrystalized, W-damaged W sample also exposed to D atoms at 600 K, from [22].

undamaged halves are shown. All TDS spectra are dominated by a single desorption peak and start above the exposure temperature of 600 K. The highest signal was obtained from the W-damaged half of the nG sample showing a desorption maximum at 740 K. The TDS signal obtained on the W-damaged HnG sample is lower than the one obtained for the nG sample and has a maximum at 800 K. The lowest desorption is obtained for the W-damaged mG sample which peaks at 840 K. In Fig. 10, we also show the D desorption signal obtained from a hot-rolled, recrystallized, 20 MeV W-irradiated tungsten sample exposed to the same D beam for a similar fluence of 1.03×10^{24} D/m^2, taken from [22]. In this case, the desorption peaks at 800 K. The desorption spectrum of recrystallized W is similar to the desorption spectrum obtained on the HnG sample. Even though the grain size of recrystallized W (10–50 μm) is closer to the mG sample, the voids observed in that sample probably influence the D desorption by shifting it to higher temperature. Integrating the desorption spectra over time gives the total D desorption. Comparing these values with the D amount within the ^{3}He-NRA information depth, we see that we detected by TDS only 55 % of the D amount seen by NRA. The fact that we lack a substantial fraction of the D amount by TDS indicates that the D must have been lost during storage. This outgassing is substantially larger for the here studied films as compared to W-damaged polycrystalline W. For recrystallized, self-damaged tungsten, exposed to D plasma at 370 K at most 6 % outgassing was observed after 1.5 years [24].

When comparing the D desorption signal from the undamaged halves, also shown in Fig. 10, the height of the D desorption peak from the undamaged nG samples is one-third of the D desorption from the damaged half exhibiting a peak position at the same temperature as the damaged half. This observation is in good agreement with the NRA-measured D concentration, obtaining the same ratio between the damaged and undamaged half. The D desorption from the undamaged halves of the HnG and mG samples is marginal compared to the damaged halves, obtaining only a small peak at 600 K. The smallest peak was obtained for the mG sample, which also agrees with the NRA-measured D depth profiles.

5. Discussion

5.1. Microstructure

We will first discuss the film properties. The high energy of the impinging species (typically up to hundreds of eV) during the PLD

process results in the formation of very compact and nanocrystalline films. The density of such PLD deposited W coatings has been estimated by several techniques such as: quartz crystal microbalance [26,50] with an estimation of 18.5 g/cm^3; Brillouin spectroscopy [51] that gives 18.2 g/cm^3; X-ray reflectometry on thin W films [52,53] that estimate density values close to the theoretical W bulk density of 19.29 g/cm^3 [39] and finally EDXS [53] that results in 18.75 g/cm^3. The last reported result leads to 97 % of the W bulk density and represents a good compromise between the above-reported results and is perfectly compatible with the presence of voids and small oxide domains found during the S/TEM analysis. The high energy of the depositing species also determines the high DL density and the presence of voids and bubble-like formation in the nG sample. The larger voids in the two annealed samples can be related to the coalescence of nano-voids during the annealing. Interestingly, the temperature coalescence of nanovoids was recently studied by De Backer et al. [54,55], where an estimate of the "diffusion temperature" as a function of the void size was given. According to [54,55], vacancy clusters of 0.5 – 1.5 nm start to move in the temperature range which agrees well with the temperature used in the present study to tailor the grain size. Moreover, the characteristics of this deposition process (i.e. the higher deposition energy compared with other PVD techniques such as magnetron sputtering) also determine an "intrinsic damage" of the growing film, which contributes significantly to the total amount of defects.

For the nG sample, where a columnar microstructure was observed, we believe that the pronounced grain size anisotropy does not affect the generation of defects because the grains and the anisotropy are small enough to allow the interstitials to diffuse in both directions. Moreover, the surface morphology (Fig. 1b,c) shows minor topology, with grooves and grain boundary ridges as a result of thermal annealing, which does not protrude into the grains. In the analysis of the cross-sections, we observed sporadic voids (porosity) on the interface between deposited W layer and bulk tungsten. The voids on the interface are scarce, and about 3 μm deep, and should not affect the D transport results since they are similar for all samples.

From the results of the XRD analysis we were able to determine the changes in micro-strain and grain size for all the different grained samples. We can conclude that annealing of "as deposited" nG W thin films leads to crystallite growth and a reduction of micro-strain. It was also observed that the crystallite size on the W-damaged halves compared to the undamaged halves for nG and HnG samples increased from 36 nm to 48 nm and from 72 nm to 144 nm, respectively. This increase is probably due to the W irradiation, where cascades cause a local heat spike and lead to an increase in grain size. This has been previously observed in tungsten [42] and other materials [56,57,58,43]. A model for radiation-induced grain growth was proposed in [57] for the low temperature regime (below about 0.15–0.22T_m), where grain growth is independent of the irradiation temperature and is based on the direct effect of the thermal spikes on the GBs. The reason for the decrease in the grain size from 289 nm to 144 nm in the case of mG is not clear, but one needs to keep in mind that XRD analysis only provides the average grain size [43]. The observed discrepancies between crystallite size estimates from SEM images and XRD method (25 nm vs. 38 nm for nG, 80 nm vs. 72 nm for HnG and 500 nm vs. 289 nm for mG, respectively) are expected and are well documented in the literature, e.g. [43]. The crystallite size calculated from XRD considers the spherical shape, and is an average of numerous (millions of) grains. On the other hand, the crystallite size estimated from the electron microscopy methods is limited to a few hundred grains, but can provide insight into the grain size distribution and also considers the shape of the crystallites (Fig. 2).

The dislocation density was determined from the TEM analysis. The determined dislocation densities for HnG and mG samples of 2.59×10^{14} m^{-2} and 2.80×10^{14} m^{-2} are in good agreement with a recent study on recrystalised tungsten with grain size of 10–100 μm [59] for similar irradiation conditions. The nG sample shows a higher dislocation density of 1.67×10^{15} m^{-2}. It is close to the one obtained on nanocrystalline tungsten irradiated with W ions by El-Atwani et al. [6].

5.2. D transport

Regarding the transport of deuterium in different-grained samples, from the above-presented depth profiles at different exposure times, one can observe a drastic change in the uptake for different grain-size samples. The nG size sample takes up D more than three times faster than the HnG sample. For the latter, D transport went a little faster than for the mG sample. The D transport is a combination of D diffusion and D trapping at the defects, as discussed in [12]. From the D concentration, we can speculate that the concentration of traps affecting the D transport is similar in all samples, yet a much faster transport was observed for the nG sample. This suggests that the effective diffusion was faster in the nG sample, implying that the GBs provide pathways for fast diffusion as predicted in [11] but opposite to the calculations of Piaggi et al. [14]. This transport difference could also be attributed to the change in the maximum D desorption peak in TDS, where a steady shift in the desorption to higher temperatures is observed when going from the nG to the mG sample. Also, the trend of D uptake is different for the studied samples. In the nG sample, D quickly penetrates down to the end of the damaged zone, and then the maximum D increases with the exposure time throughout the damage depth. In the other two cases, we see a D diffusion front moving into the bulk when increasing the exposure time. The interaction of 0.3 eV D atoms with tungsten is such that D atoms are first chemisorbed at the surface and need to overcome an energy barrier of about 2 eV [33] to enter the bulk. The faster transport for the nG sample can be either a surface effect as initially postulated in [22], as the high density of GBs at the surface could provide an additional path for atoms entering the depth, thus increasing the speed of D uptake. It could also be a bulk effect, where once atoms overcome the surface barrier, the GBs provide a faster pathway into the bulk. It could also be a combination of both. However, if the surface would be dominant, the D depth profile would grow from left to right (from surface to bulk). This is not the case for the nG but more so for the HnG or mG. If the diffusion in the GB would be bulk dominant, then the D depth profile would grow from the bottom up, which is definitely the case for nG, but not for HnG and mG. Therefore, from the D atom study alone, we can speculate that the faster diffusion is a bulk effect. Furthermore, if we compare the results obtained with D atoms with those obtained on similar thin films obtained with 300 eV/D D ions, where the surface has no direct influence on the uptake [25], we can conclude that the GBs in the bulk of the material provide faster transport of D into the depth and is therefore a bulk property.

5.3. D concentration and damage

Now, we compare the maximum D concentration of the different-grained samples. We have observed that the D concentration in the damaged zone is the highest for the nG sample. The D concentration in the HnG sample is slightly lower, and for the mG sample, it is the lowest. However, the difference is not substantial; we got 20 % higher D concentration when comparing nG and mG samples. A similar difference of 35 % between nG and mG was observed for 300 eV/D D-ion exposures at 450 K [25], where we also populated traps with lower trapping energy. Therefore, one could conclude from the present data that no significant defect annihilation was observed at the grain boundaries at room temperature. On the contrary, we observe a slight increase in the D concentration. Therefore, GBs do influence Frenkel pair annihilation but in an opposite way. Considering the low W irradiation temperature of 300 K, this can be explained by vastly different diffusion energy for self-interstitials and vacancies or vacancy clusters in tungsten, as discussed in detail in [25]. Self-interstitials have a low diffusion energy of 0.13 eV [60,61] and can migrate to the GBs during W irradiation and annihilate there. On the other hand, the vacancy diffusion energy in tungsten is high (1.85 eV) [61]; so that vacancies cannot move when created at 300

K. Diffusion energies of vacancy clusters are even larger [62,63,54]. From the TDS spectra, we observe that the maximum D desorption takes place at around 800 K, which means D populates mainly vacancy clusters, as discussed in detail in [64,63]. Therefore, during W irradiation, due to the high density of GBs, it is more probable that self-interstitials annihilate at the GBs than with vacancies or vacancy clusters, which results in a higher vacancy or vacancy cluster concentration in the vicinity of the GBs within the diffusion length of interstitials as compared to the samples with lower GB density. These conclusions agree with [8,9], where they have also observed higher hydrogen retention in nanograined samples than in micrometer-grained samples, both after irradiation. The calculations show that the formation energy for a vacancy at a GB is lower than in the bulk of tungsten [8], which also results in higher D retention for samples with a larger density of GBs. Therefore, to study the possible healing effect by enhanced vacancy annihilation at GBs in tungsten, according to [65,5,4] one would have to perform W irradiation at temperatures $\geq$600 K, where vacancies or vacancy clusters [61,62,55] become mobile and migrate, finding GBs at which they annihilate. This could be the subject of future studies. However, one needs to be aware that irradiation at elevated temperatures also produces fewer defects in polycrystalline tungsten due to defect annihilation [48,66] and the possible development of the nanocrystalline film can take place, so a good reference sample is needed that goes through the same heating/exposure procedure as the irradiated sample.

However, in our case, we also need to stress that the as-deposited thin film of the nG sample had a lot of defects due to the deposition process that were present before W-ion irradiation. We have observed even small voids/bubbles in those samples, and they then coalesce into larger voids when samples are annealed at high temperatures for tailoring the larger grain size. A significant difference in the amount of D can be also observed in Fig. 9 when comparing nG with the other two samples. We believe that this difference is due to the significant D retention beyond the damaged layer due to the initial defects in the layer. From this we can conclude that most probably in the nG sample we have simply reached saturation of defects when adding the W irradiation, similar to what was observed in [21]. Subtracting the D concentrations between the undamaged and damaged halves and comparing them, we can say that 21 % less new defects were created in the case of the nG sample compared with the mG sample. Moreover, if we subtract the amount of D measured on the undamaged half, we obtain very similar amounts of D for all samples, as can be seen in Fig. 9. Due to this large initial defect density, it is not easy to conclude how much the GBs influence defect production, but the effect is certainly not significant.

In has been shown in literature that GBs also attract hydrogen and therefore act as traps [12,15]. Since the difference in density of GBs between the nG sample and the HnG or the mG sample is much larger than the difference in the final D concentration, we can say that at the exposure temperature of 600 K, D trapping at GBs is not dominant. This is in agreement with atomic scale modelling, which suggests low binding energy of hydrogen in GBs of around 1.1 eV [10,15]. Another important observation from our measurements is that although the nG sample has an order of magnitude higher density of DL compared to HnG or mG samples, this is not reflected in the D concentration either for D atom exposures at 600 K or for D ion exposures at 450 K [25]. This therefore demonstrates the low energy trapping of hydrogen in DL as predicted by atomic scale modeling [67,68,15] and consequently is not reflected in the D concentration when loading is performed at 450 K or higher.

6. Conclusions

We have studied D retention and transport in thin W films of different grain size deposited on W substrates during exposure to 0.3 eV D atoms at 600 K. D depth profiles were measured after certain exposure times and at the end of exposure utilizing ^{3}He nuclear reaction. From our study we can clearly conclude that the D transport is the fastest in the sample with the smallest grain size. This is even true, although this sample had the highest density of defects which are known to slow down D transport. From the evolution of the D depth profile in the nanograined sample, this faster D transport can be explained as more of a bulk effect. This is even more convincing when comparing the present experiment with the experiment performed on similar W films but with 300 eV/D ions. By this we can conclude that the GBs in the bulk provide pathways for fast D diffusion. The largest D concentration was obtained on the nG sample, but the difference to the mG sample is not substantial. The increased D concentration indicates a larger density of vacancy clusters for the nG sample, which is probably due to the larger annihilation of interstitials at the grain boundaries. We can also conclude that neither the dislocations nor GBs influence D retention at 600 K. While there is a large difference in DL and GBs density, the maximum D concentration difference is only 20 % between nG and mG samples.

CRediT authorship contribution statement

S. Markelj: Conceptualization, Formal analysis, Writing – original draft, Visualization, Investigation, Recources. **J. Zavašnik:** Writing – review & editing, Investigation, Formal analysis. **A. Šestan:** Writing – review & editing, Investigation, Formal analysis. **T. Schwarz-Selinger:** Formal analysis, Writing – review & editing, Investigation. **M. Kelemen:** Investigation, Writing – review & editing. **E. Punzón-Quijorna:** Investigation, Writing – review & editing. **G. Alberti:** Investigation. **M. Passoni:** Writing – review & editing, Investigation, Resources. **D. Dellasega:** Writing – review & editing, Investigation.

Declaration of competing interest

The authors declare that they have no known competing financial interests or personal relationships that could have appeared to influence the work reported in this paper.

Data availability

Data will be made available on request.

Acknowledgements

This work has been carried out within the framework of the EUROfusion Consortium, funded by the European Union via the Euratom Research and Training Programme (Grant Agreement No 101052200 — EUROfusion). Views and opinions expressed are however those of the author(s) only and do not necessarily reflect those of the European Union or the European Commission. Neither the European Union nor the European Commission can be held responsible for them. This work was supported by IAEA Coordinated Research Project F43025, entitled ‘Hydrogen Permeation in Fusion-Relevant Materials’. The authors acknowledge the support from the Slovenian Research Agency, research core funding No. P2-0405.

Appendix A. Supplementary data

Supplementary data to this article can be found online at https://doi.org/10.1016/j.nme.2024.101589.

References

[1] T. Tanabe, Review of hydrogen retention in tungsten, Phys. Scr. T159 (2014) 014044.
[2] T. Schwarz-Selinger, A critical review of experiments on deuterium retention in displacement-damaged tungsten as function of damaging dose, Mater. Res. Express 10 (2023) 102002.
[3] X.-M. Bai, A.F. Voter, R.G. Hoagland, M. Nastasi, B.P. Uberuaga, Efficient annealing of radiation damage near grain boundaries via interstitial emission, Science 327 (2010) 1631–1634.
[4] G. Ackland, Controlling radiation damage, Science 327 (2010) 1587–1588.

[5] X.-M. Bai, B.P. Uberuaga, The influence of grain boundaries on radiation-induced point defect production in materials: A review of atomistic studies, JOM 65 (2013) 360–373.
[6] O. El-Atwani, et al., In-situ TEM/heavy ion irradiation on ultrafine-and nanocrystalline-grained tungsten: Effect of 3 MeV Si, Cu and W ions, Mater. Character. 99 (2015) 68–76.
[7] O. El-Atwani, et al., Loop and void damage during heavy ion irradiation on nanocrystalline and coarse grained tungsten: Microstructure, effect of dpa rate, temperature, and grain size, Acta Mater. 149 (2018) 206–219.
[8] G. Valles, et al., Influence of grain boundaries on the radiation-induced defects and hydrogen in nanostructured and coarse-grained tungsten, Acta Mater. 122 (2017) 277–286.
[9] M. Panizo-Laiz, et al., Experimental and computational studies of the influence of grain boundaries and temperature on the radiation-induced damage and hydrogen behavior in tungsten, Nucl. Fusion 59 (2019) 086055.
[10] H.-B. Zhou, et al., Investigating behaviours of hydrogen in a tungsten grain boundary by first principles: from dissolution and diffusion to a trapping mechanism, Nucl. Fusion 50 (2010) 025016.
[11] U. von Toussaint, S. Gori, S. Modeling hydrogen transport in large disordered systems, Phys. Scr. T159 (2014).
[12] T. Oda, Thermodynamic model for grain boundary effects on hydrogen solubility, diffusivity and permeability in poly-crystalline tungsten, Fusion Eng. Des. 112 (2016) 102–116.
[13] P. Díaz-Rodríguez, et al., Direct observation of hydrogen permeation through grain boundaries in tungsten, Emergent Mater 5 (2022) 1075–1087.
[14] P.M. Piaggi, et al., Hydrogen diffusion and trapping in nanocrystalline tungsten, J. Nucl. Mater. 458 (2015) 233–239.
[15] A. Bakaev, D. Terentyev, E.E. Zhurkin, Ab initio study of the stability of H-He clusters at lattice defects in tungsten, Nucl. Instrum. Methods Phys. Res. Sect. B: Beam Interact. Mater. Atoms 478 (2020) 269–327.
[16] K. Heinola, T. Ahlgren, K. Nordlund, J. Keinonen, Hydrogen interaction with point defects in tungsten, Phys. Rev. B 82 (2010) 094102.
[17] A. Oudriss, et al., Grain size and grain-boundary effects on diffusion and trapping of hydrogen in pure nickel, Acta Mater. 60 (2012) 6814–6828.
[18] A. Oudriss, J. Creus, J. Bouhattate, C. Savall, B. Peraudeau, X. Feaugas, The diffusion and trapping of hydrogen along the grain boundaries in polycrystalline nickel, Scr. Mater. 66 (2012) 37–40.
[19] B. Osman Hoch, A. Metsue, J. Bouhattate, X. Feaugas, Effects of grain-boundary networks on the macroscopic diffusivity of hydrogen in polycrystalline materials, Comput. Mater. Sci 97 (2015) 276–284.
[20] J. Li, et al., Antagonist effects of grain boundaries between the trapping process and the fast diffusion path in nickel bicrystals, Sci Rep 11 (2021) 15533.
[21] O.V. Ogorodnikova, Effect of nanostructure on radiation tolerance and deuterium retention in tungsten, J. Appl. Phys. 122 (2017) 044902.
[22] M. Pečovnik, S. Markelj, A. Založnik, T. Schwarz-Selinger, Influence of grain size on deuterium transport and retention in self-damaged tungsten, J. Nucl. Mater. 513 (2019) 198.
[23] O.V. Ogorodnikova, V. Gann, Simulation of neutron-induced damage in tungsten by irradiation with energetic self-ions, J. Nucl. Mater. 460 (2015) 60.
[24] B. Wielunska, M. Mayer, T. Schwarz-Selinger, A.E. Sand, W. Jacob, Deuterium retention in tungsten irradiated by different ions, Nucl. Fusion 60 (2020) 096002.
[25] S. Markelj, et al., The effect of nanocrystalline microstructure on deuterium transport in displacement damaged tungsten, Nucl. Mater. Energy 37 (2023) 101509.
[26] D. Dellasega, G. Merlo, C. Conti, C.E. Bottani, M. Passoni, Nanostructured and amorphous-like tungsten films grown by pulsed laser deposition, J. Appl. Phys. 112 (2012) 084328.
[27] A. Pezzoti, "Tungsten-based coatings for magnetic fusion research: damage and hydrogen retention," PhD thesis, Politecnico Milano, Milano https://www.politesi.polimi.it/handle/10589/132679., 2017.
[28] T. Schwarz-Selinger, Deuterium retention in MeV self-implanted tungsten: influence of damaging dose rate, Nucl. Energy Mater. 12 (2017) 683–688.
[29] J. Ziegler, "www.srim.org.," [Online].
[30] D.R. Mason, et al., Parameter-free quantitative simulation of high-dose microstructure and hydrogen retention in ion-irradiated tungsten, Phys. Rev. Mater. 5 (2021).
[31] S. Markelj, A. Založnik, T. Schwarz-Selinger, O.V. Ogorodnikova, P. Vavpetič, P. Pelicon, I. Čadež, In situ NRA study of hydrogen isotope exchange in self-ion damaged tungsten exposed to neutral atoms, J. Nucl. Mater. 469 (2016) 133–144.
[32] S. Markelj, O.V. Ogorodnikova, P. Pelicon, T. Schwarz-Selinger, I. Cadez, Temperature dependence of D atom adsorption on polycrystalline tungsten, Appl. Surf. Sci. 282 (2013) 478–486.
[33] E.A. Hodille, A. Založnik, S. Markelj, T. Schwarz-Selinger, C.S. Becquart, R. Bisson, C. Grisolia, Simulations of atomic deuterium exposure in self-damaged tungsten, Nucl. Fusion 57 (2017) 056002.
[34] A. Založnik, S. Markelj, T. Schwarz-Selinger, Ł. Ciupiński, J. Grzonka, P. Pelicon, The influence of the annealing temperature on deuterium retention in self-damaged tungsten, Phys. Scr. T167 (2016).
[35] A. Založnik, S. Markelj, T. Schwarz-Selinger, K. Schmid, Deuterium atom loading of self-damaged tungsten at different sample temperatures, J. Nucl. Mater. 496 (2017) 1–8.
[36] E. Hodille, S. Markelj, T. Schwarz-Selinger, A. Zaloznik, M. Pecovnik, M. Kelemen, C. Grisolia, Stabilization of defects by the presence of hydrogen in tungsten: simultaneous W-ion damaging and D-atom exposure, Nucl. Fusion 59 (2019) 016011.
[37] B. Wielunska, M. Mayer, T. Schwarz-Selinger, U. von Toussaint, J. Bauer, Cross Section Data for the D(^{3}He, p)^{4}He Nuclear Reaction from 0.25 to 6 MeV, Nucl. Instr. Meth. Phys. Res. B 371 (2016) 61.
[38] K. Schmid, U. von Toussaint, Nucl. Instr. Meth. Phys. Res. B 281 (2012) 64.
[39] M. Meyer, "SIMNRA User's Guide, Report IPP 9/113," Max-Planck-Instutut für Plasmaphysik, Garching, Germany, 1997. [Online]. Available: http://www.rzg.mpg.de/~mam/.
[40] M. Guitart Corominas, T. Schwarz-Selinger, Experimental determination of the ^{16}O (^{3}He, p_0)^{18}F differential cross section, Nucl. Instr. and Meth. Phys. Res. B 450 (2019) 13–18.
[41] J. Pelleg, E. Elish, D. Mogilyanski, Evaluation of average domain size and microstrain in a silicide film by the Williamson-Hall method, Metall Mater Trans A 36 (2005) 3187–3194.
[42] M.L. Khalid, et al., Effect of carbon ion irradiation on the structural, mechanical and electrical properties of polycrystalline tungsten, Mater. Res. Express 6 (2019) 066551.
[43] W. Mohamed, B. Miller, D. Porter, K. Murty, The role of grain size on neutron irradiation response of nanocrystalline copper, Materials 9 (2016) 144.
[44] E. Salançon, T. Dürbeck, T. Schwarz-Selinger, F. Genoese, W. Jacob, Redeposition of amorphous hydrogenated carbon films during thermal decomposition, J. Nucl. Mater. 376 (2008) 160–168.
[45] T. Schwarz-Selinger, J. Bauer, S. Elgeti, S. Markelj, Influence of the presence of deuterium on displacement damage in tungsten, Nucl. Mater. Energy (2018) 228–234.
[46] K. Kremer, M. Brucker, W. Jacob, T. Schwarz-Selinger, Influence of thin surface oxide films on hydrogen isotope release from ion-irradiated tungsten, Nucl. Mater. Energy 30 (2022) 101137.
[47] A. Šestan, P. Jenuš, S. Krmpotič, J. Zavašnik, J. Zavašnik, M. Čeh, The role of tungsten phases formation during tungsten metal powder consolidation by FAST: Implications for high-temperature application, Mater. Charact. 138 (2018) 308–314.
[48] S. Markelj, T. Schwarz Selinger, A. Zaloznik, M. Kelemen, P. Vavpetic, P. Pelicon, E. Hodille, C. Grisolia, Deuterium retention in tungsten simultaneously damaged by high energy W ions and loaded by D atoms, Nucl. Mater. Energ. 12 (2017) 169–174.
[49] S. Markelj, et al., Deuterium transport and retention in the bulk of tungsten containing helium: the effect of helium concentration and microstructure, Nucl. Fusion 60 (2020) 106029.
[50] M.H.J. 't Hoen, et al., Deuterium retention and surface modifications of nanocrystalline tungsten films exposed to high-flux plasma, J. Nucl. Mater. 463 (2015) 989–992.
[51] E. Besozzi, et al., Amorphous, ultra-nano- and nano-crystalline tungsten-based coatings grown by pulsed laser deposition: mechanical characterization by surface brillouin spectroscopy, Mater. Des. 106 (2016) 14–21.
[52] D. Dellasega, et al., High energy pulsed laser deposition of ohmic tungsten contacts on silicon at room temperature, Thin Solid Films 666 (2018) 121–129.
[53] A. Pazzaglia, A. Maffini, D. Dellasega, A. Lamperti, Reference-free evaluation of thin films mass thickness and composition through energy dispersive X-ray spectroscopy, Mater Charact 153 (2019) 92–102.
[54] A. De Backer, et al., Multi-objective optimization of the nanocavities diffusion in irradiated metals, Phys. Sci. Forum 5 (2023) 41.
[55] A. De Backer, et al., Readdressing nanocavity diffusion in tungsten, Front. Nucl. Eng. 2 (2023).
[56] D. Kaoumi, A.T. Motta, R.C. Birtcher, Grain growth in Zr–Fe thin films during in situ ion irradiation in a TEM, Nucl. Instrum. Methods Phys. Res., Sect. B 242 (2006) 490–493.
[57] D. Kaoumi, A.T. Motta, R.C. Birtcher, A thermal spike model of grain growth under irradiation, J. Appl. Phys. 104 (2008) 073525.
[58] M. Thomas, et al., Thermal and radiation stability in nanocrystalline Cu, Nanomaterials (Basel) 12 (2023) 1211.
[59] S. Wang and e, et al., Dynamic equilibrium of displacement damage defects in heavy-ion irradiated tungsten, Acta Mater. 244 (2023) 118578.
[60] P.M. Derlet, D. Nguyen-Manh, S.L. Dudarev, Multiscale modeling of crowdion and vacancy defects in body-centered-cubic transition metals, Phys. Rev. B 76 (2007) 054107.
[61] J. Heikinheimo, et al., Direct observation of mono-vacancy and self-interstitial recovery in tungsten, APL Mater. 7 (2019) 021103.
[62] D.R. Mason, D. Nguyen-Manh, C.S. Becquart, An empirical potential for simulating vacancy clusters in tungsten, J. Phys.: Condens. Matter 29 (2017) 505501.
[63] M. Pečovnik, et al., Effect of D on the evolution of radiation damage in W during high temperature annealing, Nucl. Fusion 60 (2020) 106028.
[64] M. Pečovnik, S. Markelj, E. Hodille, T. Schwarz-Selinger, C. Grisolia, New rate equation model to describe displacement damage stabilization by hydrogen atoms in tungsten, Nucl. Fusion 60 (2020) 036024.
[65] I.J. Beyerlein, et al., Radiation damage tolerant nanomaterials, Mater. Today 16 (2013) 443–449.
[66] S. Markelj, et al., Displacement damage stabilization by hydrogen presence under simultaneous W ion damage and D ion exposure, Nucl. Fusion 59 (2019) 086050.
[67] A. Bakaev, P. Grigorev, D. Terentyev, A. Bakaeva, E.E. Zhurkin, A. Mastrikov, Trapping of hydrogen and helium at dislocations in tungsten: an ab-initio study, Nucl. Fusion 57 (2017) 126040.
[68] A. De Backer, et al., Hydrogen accumulation around dislocation loops and edge dislocations: from atomistic to mesoscopic scales in BCC tungsten, Phys. Scr. T170 (2017) 014073.